Supporting Information

Self-Purifying Chloride-Mediated Sequential Nitrate Reduction-Oxidation Enabled by a Co-Oxygen Vacancy Tandem Photoelectrocatalyst

Yue He,[a] Hongbao Jia,[c] Ziyan Zhang,[a] Jiale Wang,[a] Xinyu Deng,[a] Jinghuan Peng,[a] Jue Wu,[b] Hui Xu,[a] Ding Wang,[a] Huan Shang,[a] Guisheng Li[a]*

[a]School of Materials and Chemistry, University of Shanghai for Science and Technology, Shanghai 200093, P. R. China.

[b]Department of Mathematics and Science, Fujian Jiangxia University, Fuzhou, 350108, China.

[c]School of Chemical Science and Engineering, Tongji University, Shanghai 200092, China.

*Corresponding authors: huanshang1992@163.com.

CONTENTS: 44 pages, 8 texts, 32 figures and 1 table

Texts

Figures

Figure S12. Corresponding plots of transformed Kubelka-Munk function versus photon energy of Co-OV/TiO_2@TP and NTO@TP.

Figure S13. The schematic diagram of band structures of Co-OV/TiO_2@TP and NTO@TP.

Figure S14. Transient photocurrent responses of Co-OV/TiO_2@TP and NTO@TP. Figure S15. EIS of as-prepared Co-OV/TiO_2@TP, NTO@TP and TiO_2@TP.

Figure S16. (a) Room-temperature steady-state PL spectra, (b) The corresponding PL decay curves of Co-OV/TiO_2@TP and NTO@TP.

Figure S17. (a) UV−vis absorption spectra of various concentration gradients of NO_3^--N. (b) The concentration-absorbance calibration curves of NO_3^--N.

Figure S18. (a) UV−vis absorption spectra of various concentration gradients of NO_2^--N. (b) The concentration-absorbance calibration curves of NO_2^--N.

Figure S19. (a) UV−vis absorption spectra of various concentration gradients of NH_4^+-N. (b) The concentration-absorbance calibration curves of NH_4^+-N.

Figure S20. At different potentials by Co-OV/TiO_2@TP for 4h in 50 mg L^{-1} NO_3^--N, 0.03 M KCl and 0.1 mol L^{-1} K_2SO_4 solution.

Figure S21. Photo-electrocatalytic NO_3^--N conversion and N_2 selectivity of Co-TiO_2@TP.

Figure S22. Characterization and NO_3RR performance of TiO_2-OV/TP prepared by Ar calcination. (a) XRD pattern, (b) EPR spectrum, and (c) NO_3^--N conversion and N_2 selectivity.

Figure S23. CV curves at the scan rates changed from 20 to 100 mV s^{-1}. Cyclic voltammetry curves of (a) Co-OV/TiO_2@TP, (b) and NTO@TP (c) TiO_2@TP electrodes. (d) Plots of half of the current density difference ($\Delta j/2$) at the centered potential plotted against the scan rate. The slope of fitted straight line is the C_{dl} value.

Figure S24. (a) Time-resolved concentration evolution of nitrogen species during the PEC NO_3RR over Co-OV/TiO_2@TP at 1.5 V vs.SCE in 0.1 mol L^{-1} K_2SO_4 and 0.03 M KCl solution with initial concentration of 50 mg L^{-1} NO_3^--N. The dashed line indicates the WHO drinking

Table

Text S1. Physical characterizations.

The surface morphology and elemental distribution of electrocatalysts were observed using a field emission scanning electron microscope (SEM, ZEISS Merlin Compact; Jena; Germany) equipped with an energy dispersive spectrometer (EDS) and transmission electron microscope (TEM, JEOL JEM-2100; Tokyo; Japan) equipped with EDS. The TEM images were recorded on a Thermo Scientific Talos F200X microscope with an accelerating voltage of 200 kV. X-ray diffraction (XRD) for the crystalline phase was obtained with a Bruker D8 Advance operated at 40 kV and 30 Ma at a canning rate of 5° min^{-1}. Raman spectra were collected on a HORIBA Lab RAM HR Evolution with an Ar ion laser as an excitation source ($\lambda = 532$ nm). The Co content was analyzed by dissolving the samples in 2 mols/L HNO_3 and measuring Co concentration resulting solution using inductive coupled plasma optical emission spectrometer (ICP OES, iCAP 7000 Series, Thermo Fisher iCAP PRO).The nitrogen adsorption-desorption isotherms were measured using a BET analyzer (Micromeritics ASAP 2460). Microstructure characteristics were obtained by transmission electron microscopy with a Hitachi H-7650. X-ray photoelectron spectroscopy (XPS, Thermo Scientific K-Alpha) with a monochromatized Al Kα line source (200W) was used to investigate the surface structure. UV-vis Diffuse Reflectance Spectra (UV-vis DRS, UV2600, Shimadzu, Japan) were used to analyze the adsorption properties of samples. Photoluminescence (PL) spectra were performed on the FLS1000 fluorescence spectrophotometer to probe the sample's optical properties. The detection of Ov and *H was conducted on an EPR spectroscope (Bruker EMX Nano, Germany). DMPO was applied as the spin-trapping agent of *H. Samples were collected after 5 min photoelectrolysis at a current density of 5 mA/cm^2, mixed with DMPO and transferred into a quartz tube for EPR measurement.

Text S2. Photoelectrochemical measurements.

The photoelectrochemical test was performed by using a CHI 660D instrument (Shanghai CHI Instruments Co.) which is equipped with a standard three-electrode cell system (diaphragmless single-cell device). The counter electrode was a platinum plate,

the reference electrode was saturated glycogen electrode (SCE), and the working electrode was as-prepared Co-OV/TiO_2@TP photoelectrode (the geometric area: 2 cm × 2 cm). 0.1 M K_2SO_4 and 0.03 M KCl was used as the electrolyte. To simulate sunlight (100 $mW \cdot cm^{-2}$), the solar simulator was employed (AM 1.5 G, ABET TECHNOLOGIES). The single-cell were filled with 70 ml solution (0.1 M K_2SO_4 + 0.03 M KCl +50 mg L^{-1} NO_3^--N) and then degassed by Ar (99.999%) for more than 30 mins. Linear sweep voltammetry (LSV) was recorded at a scan rate of 5 mV/s for the NO_3RR process. Electrochemical impedance spectroscopy (EIS) measurements were performed in the range from 100 kHz to 0.01 Hz with a perturbation of 5 mV amplitude. To estimate the C_{dl}, cyclic voltammetry (CV) was carried out in the non-Faradaic potential region from -0.21 to -0.09 V vs. SCE with various scan rates, and then the capacitive current $\Delta j = (ja - jc)/2$ at -0.15 V was plotted versus the scan rate. Chronoamperometry (i-t) tests were performed to measure the current response at a constant potential. The photoelectrocatalytic activity of NO_3RR at Co-OV/TiO_2@TP cathode was evaluated under different conditions, such as electrocatalytic applied potentials (-1.2, -1.3, -1.4, 1.5 and -1.6 V vs. SCE), electrolyte type, (K_2SO_4 and KCl) solution pH (3.0, 5.0, 7.0, 9.0, 11.0), and NO_3^--N concentration (10, 20, 50 and 100 mg L^{-1}), and the pH of the solution was adjusted using hydrochloric acid and potassium hydroxide.

Text S3. In-situ IR measurements.

In-situ FTIR spectra were collected on an iS50 FTIR spectrometer with substrate monocrystallinesilicon ingot. 2.0 mg of Co-OV/TiO_2@TP catalyst and 10 μL of Nafion solution were added to 200 μL of ethanol and 400 μL of deionized water, and then ultrasonicated for 1 hour to obtain a uniform ink. 600 μL of the ink was carefully dropped onto a carbon paper as the working electrode. The copper wire and the saturated calomel electrode were used as the counter electrode and the reference electrode respectively. Then, 0.1 M K_2SO_4 solution and 0.03 M KCl and 50 ppm NO_3^--N were used as the electrolytes. Before measurement, the background spectrum of the working electrode at open-circuit voltage was recorded. At a voltage of -0.8 V vs SCE,

in-situ Fourier Transform Infrared Spectroscopy was continuously measured every 100 seconds.

Text S4. In-situ Raman measurements.

The measurements were performed on a HORIBA Lab RAM HR Evolution coupled with a CHI 660 electrochemical workstation. A Co-OV/TiO_2@TP electrode coated with catalyst powder served as the working electrode during the experiments. This electrode was immersed into the electrolyte via the cell wall, ensuring the electrode surface remained perpendicular to the laser beam. A copper wire and an Ag/AgCl electrode were employed as the counter electrode and reference electrode, respectively. The electrochemical environment consisted of electrolyte containing 50 mg L^{-1} NO_3^--N, 0.1 mol/L K_2SO_4, and 0.03 mol/L KCl. Chronoamperometry (i-t) tests were conducted at each fixed potential for 300 seconds.

Text S5. Differential electrochemical mass spectrometry (DEMS) measurements.

0.1 M K_2SO_4 and 0.03 M KCl electrolyte solution containing 50 ppm NO_3^--N was continuously pumped into a custom-designed electrochemical cell using a peristaltic pump. Before and during DEMS measurements, Ar (99.999%) was continuously purged through the electrolyte. Potential sweeps from 0 V to -2.0 V (vs.SCE) were performed at 10 mV/s until baseline stabilization was achieved, with simultaneous recording of corresponding mass spectrometry signals. Three consecutive runs were conducted under identical conditions to minimize random errors in DEMS measurements, concluding the experimental procedure after the three cycles.

Text S6. Product analysis.

Determination of nitrate-N (NO_3^--N):The electrolyte solution was collected and filtered through a 22 μm aqueous-phase membrane, then quantitatively diluted to 5 mL with deionized water (within the detection range). Subsequently, 200 μL of 1 M HCl and 20 μL of sulfamic acid solution (0.8% w/v) were sequentially added to the diluted solution. After standing for 5 minutes, the UV-Vis absorption spectrum was measured, and the absorption intensities at 220 nm and 275 nm were recorded. The concentration of NO_3^--N was calculated by the absorbance value A (A=A220 nm-2A275 nm). A

calibration curve relating absorbance to concentration was established using standard potassium nitrate solutions (Figure S17 in Supporting Information), and the potassium nitrate crystal was dried at 105-110 ℃ for 2 h in advance.

Determination of nitrite-N (NO_2^--N): A color reagent was prepared by mixing 4 g of p-aminobenzenesulfonamide, 0.2 g of N-(1-Naphthyl) ethylenediamine dihydrochloride, 50 mL of ultrapure water, and 10 mL of phosphoric acid (ρ = 1.70 g/mL), followed by dilution to a final volume of 100 mL. An aliquot of the electrolyte solution was collected, filtered through a 0.22 μm aqueous-phase membrane, and quantitatively diluted to 5 mL with deionized water (within the detection range). Subsequently, 0.1 mL of the color reagent was added to the diluted solution, mixed thoroughly, and allowed to stand for 20 min. The absorption intensity at 540 nm was recorded. A concentration-absorbance calibration curve was established using a series of standard sodium nitrite solutions (Fig. S18 in Supporting Information).

Determination of NH_4^+-N: Ammonia-N was determined using Nessler's reagent as the color agent. An aliquot of the electrolyte solution was filtered through a 0.22 μm aqueous-phase membrane filter and quantitatively diluted to 5 mL with deionized water (within the detection range). Subsequently, 0.1 mL of potassium sodium tartrate solution and 0.1 mL of Nessler's reagent were sequentially added to the diluted solution. After thorough mixing and standing for 15 min, the UV-Vis absorption spectrum was measured, and the absorption intensity at 420 nm was recorded. A concentration-absorbance calibration curve was established using a series of standard ammonium chloride solutions and the ammonium chloride crystal was dried at 100℃ for 2 h in advance (Fig. S19 in Supporting information). The potassium sodium tartrate solution was prepared by dissolving 50 g of potassium sodium tartrate tetrahydrate ($KNaC_4H_4O_6 \cdot 4H_2O$) in 100 mL of ultrapure water, heated to boiling to remove residual ammonium ions, cooled to room temperature, and diluted to a final volume of 100 mL.

Text S7. Calculation of nitrate conversion and product selectivity.

The conversion of NO_3^- was calculated:

199 $$C(NO_3^-)\% = \frac{C_0(NO_3^- - N) - C_t(NO_3^- - N)}{C_0(NO_3^- - N)} \times 100\%$$

200 The selectivity of the product was calculated:

201 $$S(N_2)\% = \frac{C_0(NO_3^- - N) - C_t(NO_2^- - N) - C_t(NH_4^+ - N)}{\Delta C(NO_3^- - N)} \times 100\%$$

202 Where C_0 (NO_3^-) (mg L^{-1}) and C_t (NO_3^-) (mg L^{-1}) are the initial nitrate (NO_3^--N)
203 concentration and nitrate concentration after different electrocatalytic reduction time,
204 respectively. C_t (NO_2^--N) and C_t (NH_4^+-N) represent the concentrations of nitrite and
205 ammoniums.

206 **Text S8.** Theoretical simulations.

207 The spin-polarized density functional theory (DFT) calculations were obtained by
208 the Vienna Ab initio Simulation Package where the implemented projector augmented
209 wave method was used to describe the wave function.[1-3] The Perdew-Burke-Ernzerhof
210 density function with generalized gradient approximation was employed for the
211 exchange-correlation energy,[4] in which the Hubbard U correction was 6 eV for 3d
212 electrons of Ti atoms for the total relaxation and the plane wave cutoff was 400 eV.
213 The Brillouin-zone integrations were approximated by using the Monkhorst-Pack
214 scheme.[5] The wave function optimization was terminated when energy change was
215 converged to 10^{-5} eV and corresponding ionic relaxation loop to 0.02 eV $Å^{-1}$. The TiO_2
216 (101) surface models with Fe single-atom were adopted to simulate O_2/NO adsorption
217 with the periodic vacuum of 20 Å.

218

219

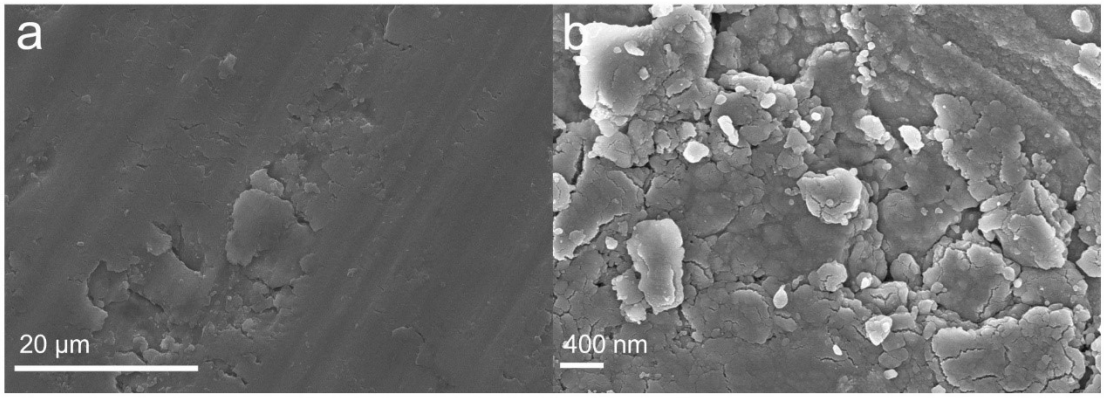

220

221 **Figure S1.** SEM images of (a) TP, (b) TiO_2@TP.

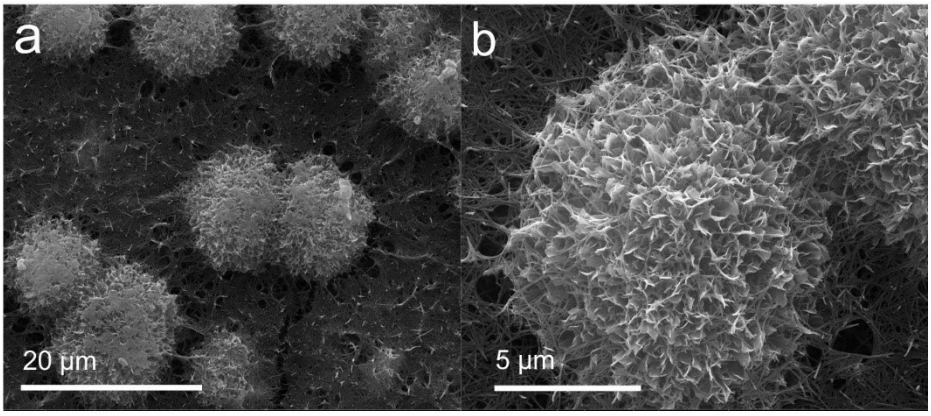

222

223 **Figure S2**. SEM image of NTO@TP at (a) 20 um and (b) 5 um.

224

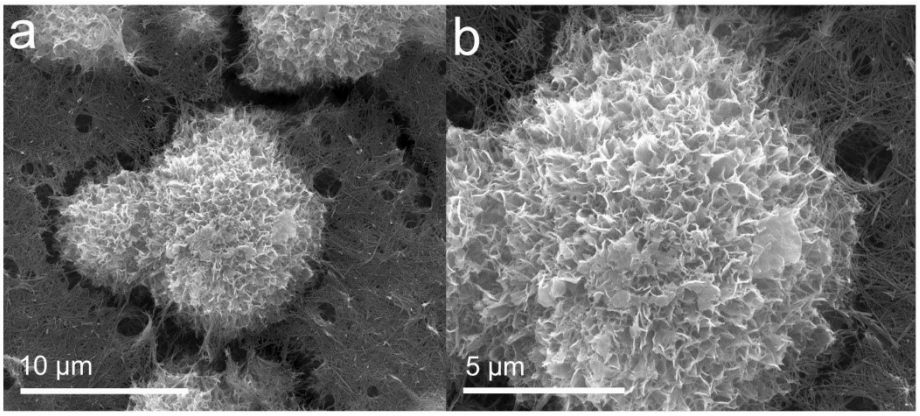

225

226 **Figure S3.** SEM image of Co-OV/TiO_2@TP at (a) 10 um and (b) 5 um.

227

228

229

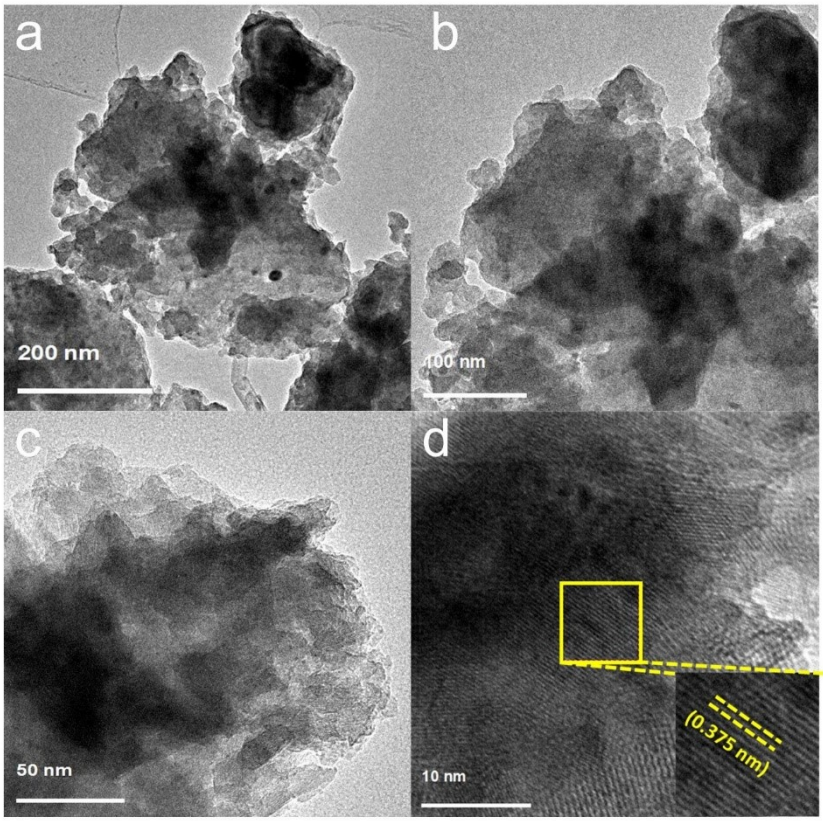

230 **Figure S4.** (a-c) TEM and (d) HRTEM images of NTO@TP.

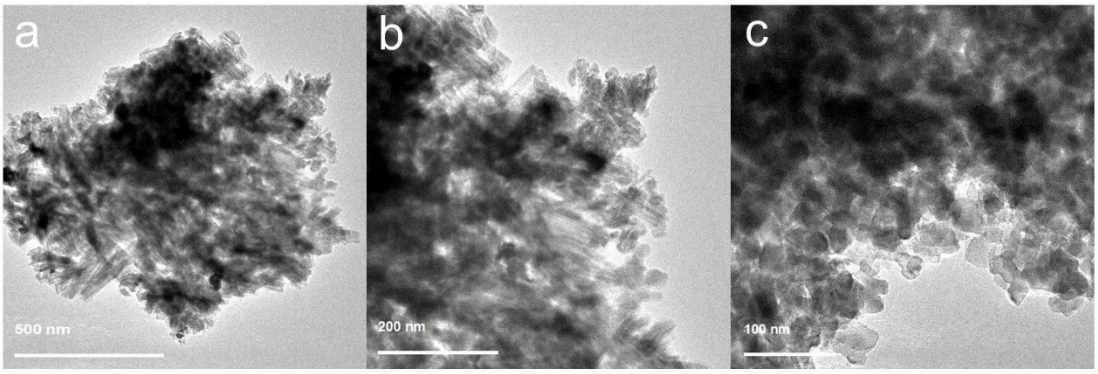

231

232 **Figure S5.** TEM image of Co-OV/TiO_2@TP at (a) 500 nm, (b) 200 nm, and 100 nm.

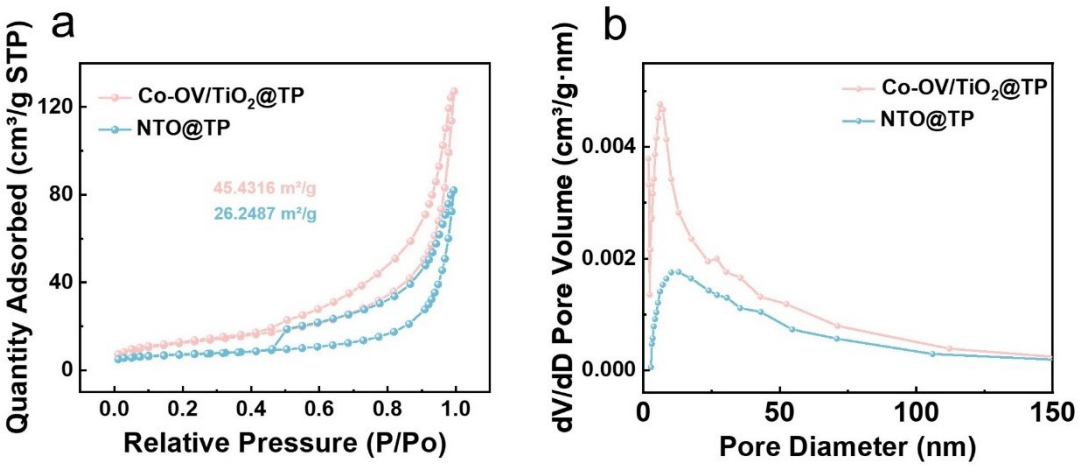

233

234 **Figure S6.** (a) N_2 adsorption-desorption isotherms, (b) Corresponding pore size distribution
235 curves.

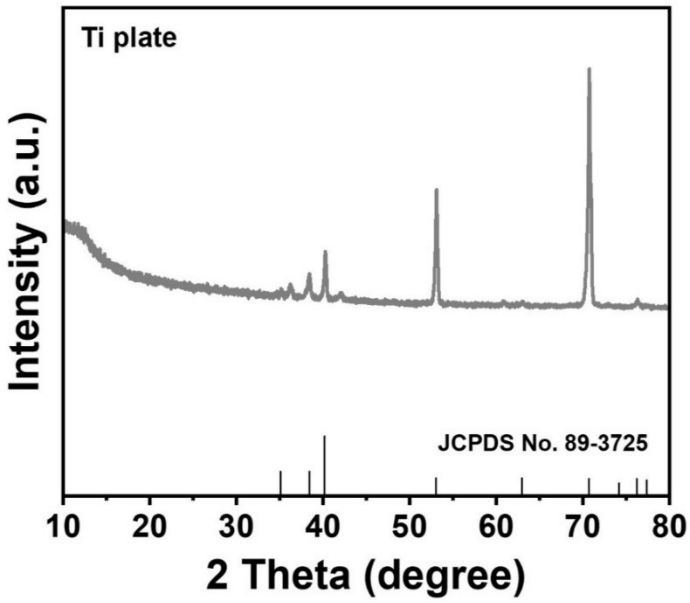

236

237 **Figure S7**. XRD pattern of TP.

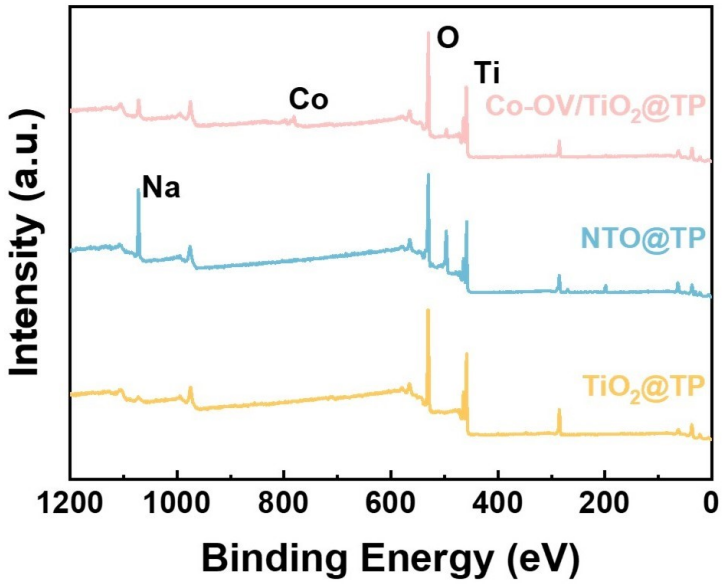

238

239 **Figure S8.** XPS survey analysis of Co-OV/TiO_2@TP@TP, NTO@TP and TiO_2@TP.

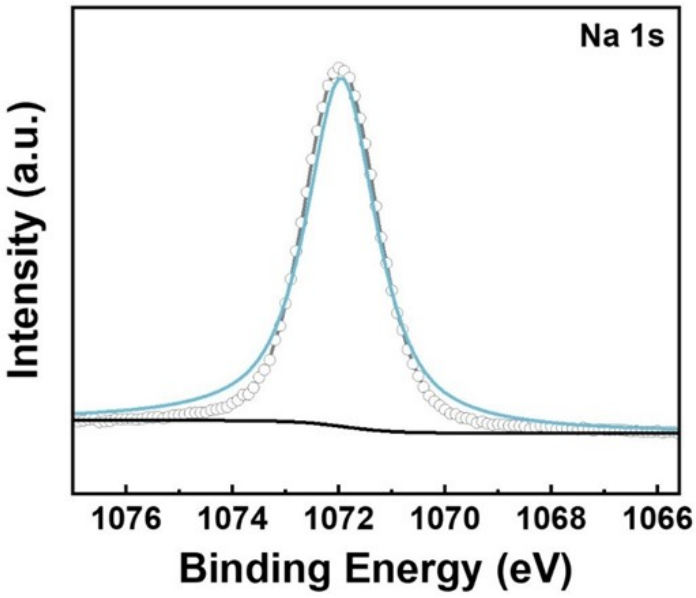

240

241 **Figure S9.** High-resolution XPS spectra of Na 1s of NTO@TP.

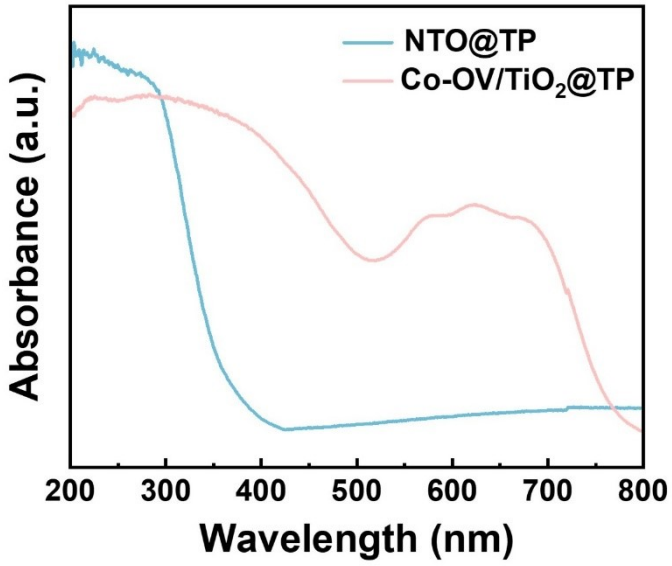

242

243 **Figure S10.** (a) UV–vis DRS spectra of Co-OV/TiO_2@TP and NTO@TP.

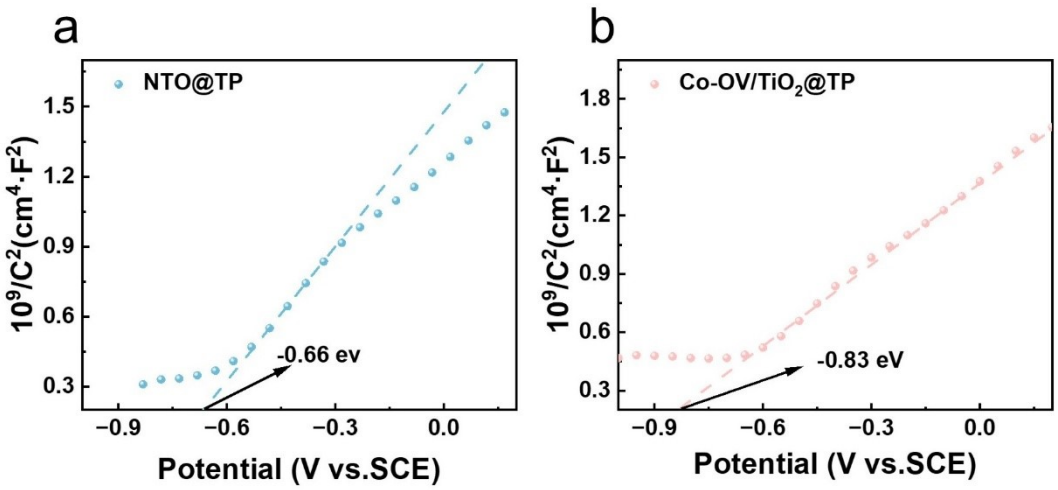

244

245 **Figure S11.** Mott-Schottky plots of (a) NTO@TP and (b) Co-OV/TiO_2@TP.

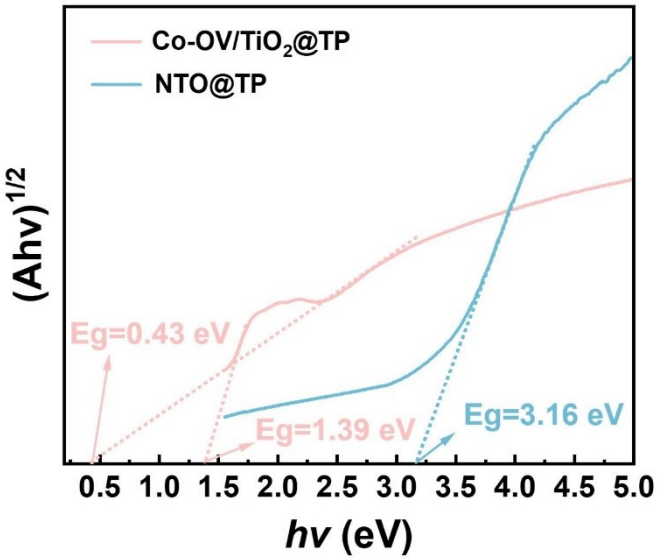

246

247 **Figure S12.** Corresponding plots of transformed Kubelka-Munk function versus photon energy
248 of Co-OV/TiO_2@TP and NTO@TP.

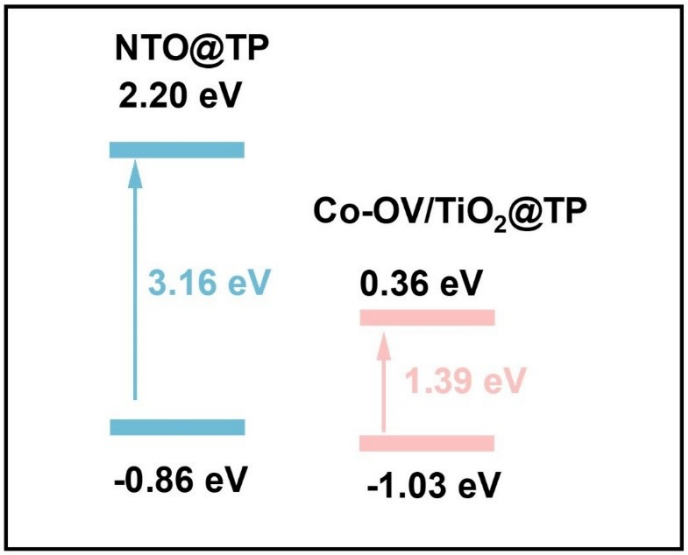

249

250 **Figure S13.** The schematic diagram of band structures of Co-OV/TiO_2@TP and NTO@TP.

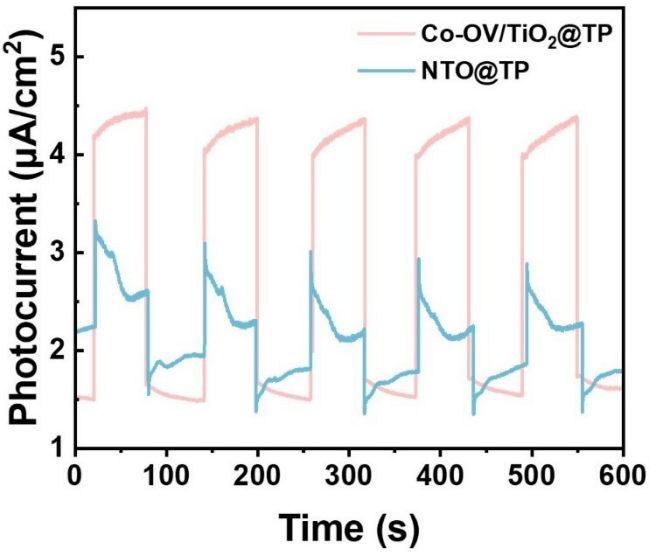

251

252 **Figure S14.** Transient photocurrent responses of Co-OV/TiO_2@TP and NTO@TP.

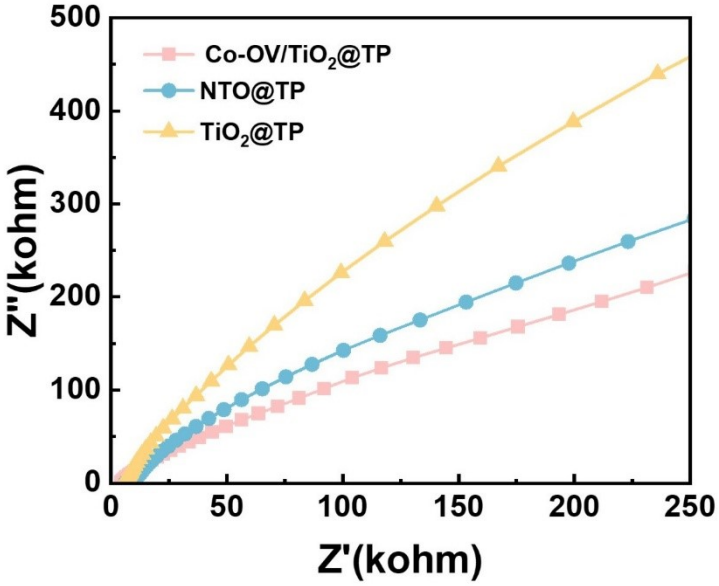

253

254 **Figure S15.** EIS of as-prepared Co-OV/TiO_2@TP, NTO@TP and TiO_2@TP.

255

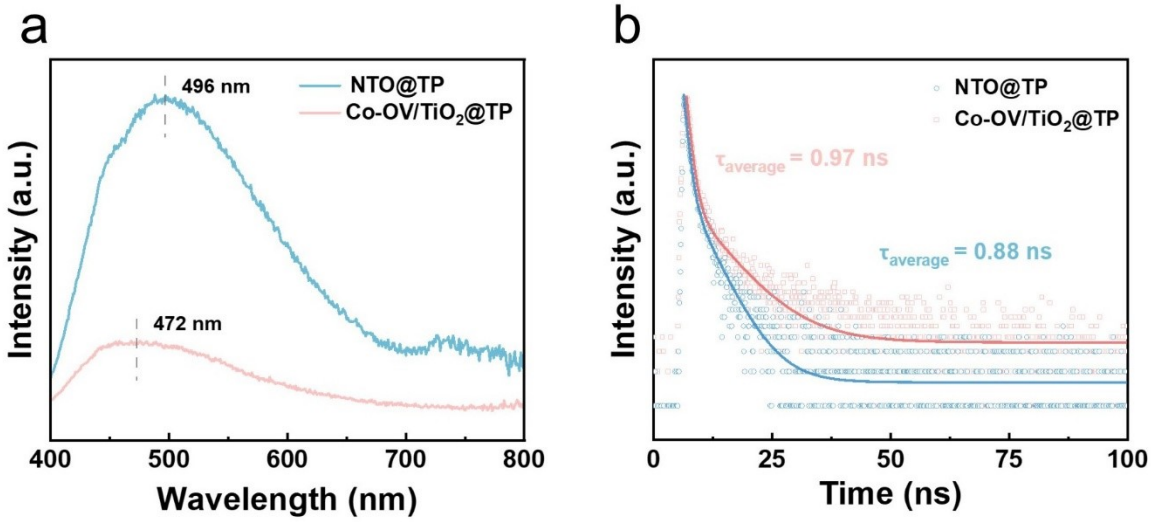

256

257 **Figure S16.** (a) Room-temperature steady-state PL spectra, (b) The corresponding PL decay
258 curves of Co-OV/TiO_2@TP and NTO@TP.

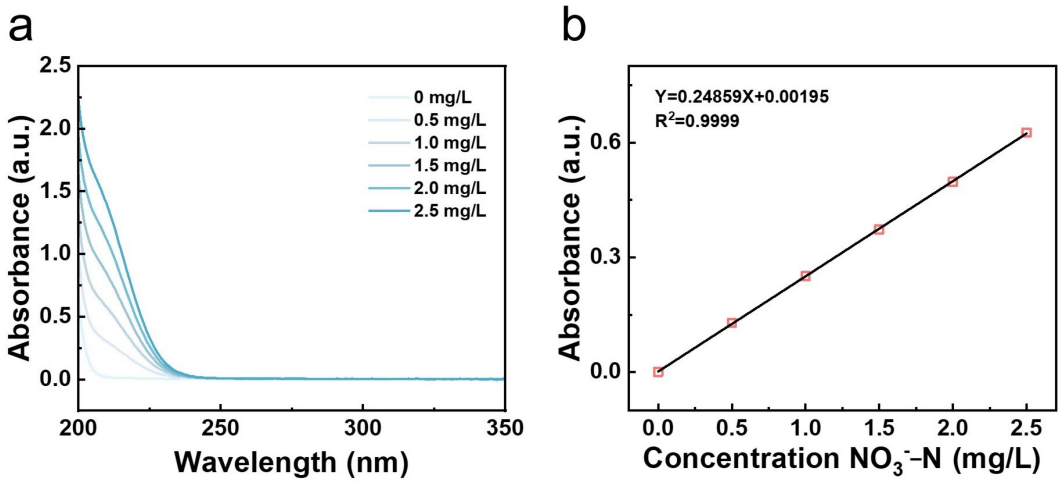

259

260 **Figure S17.** (a) UV−vis absorption spectra of various concentration gradients of NO_3^--N. (b)
261 The concentration-absorbance calibration curves of NO_3^--N.

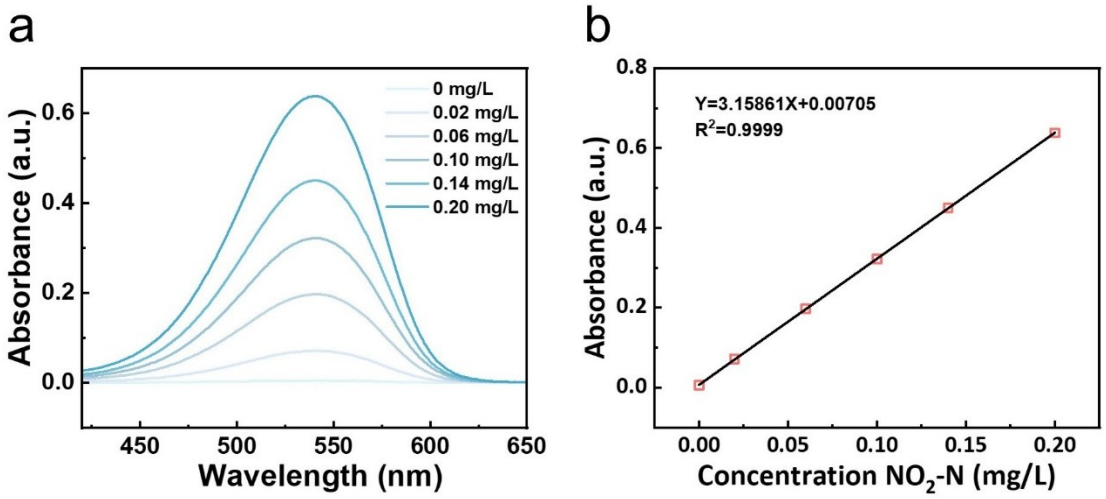

262

263 **Figure S18.** (a) UV−vis absorption spectra of various concentration gradients of NO_2^--N. (b)
264 The concentration-absorbance calibration curves of NO_2^--N.

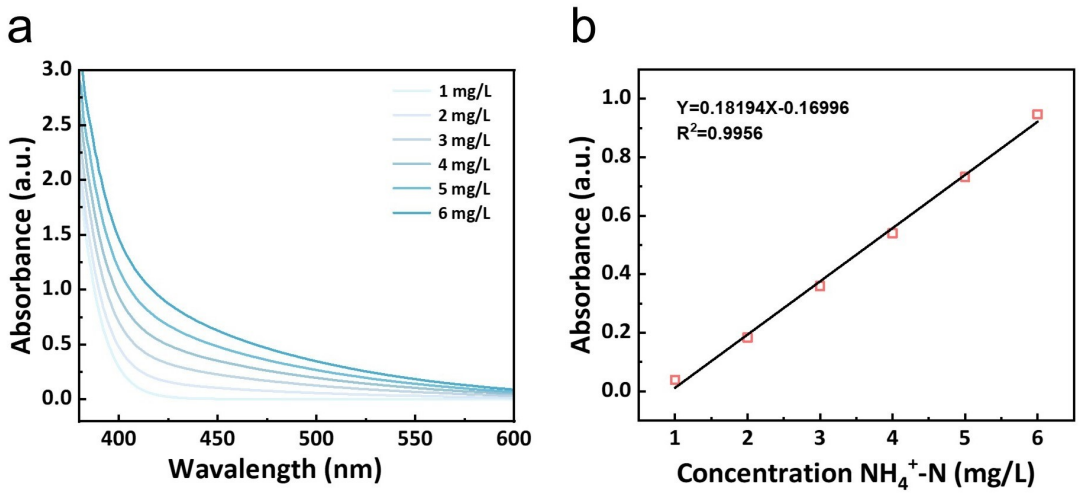

Figure S19. (a) UV−vis absorption spectra of various concentration gradients of NH_4^+-N. (b) The concentration-absorbance calibration curves of NH_4^+-N.

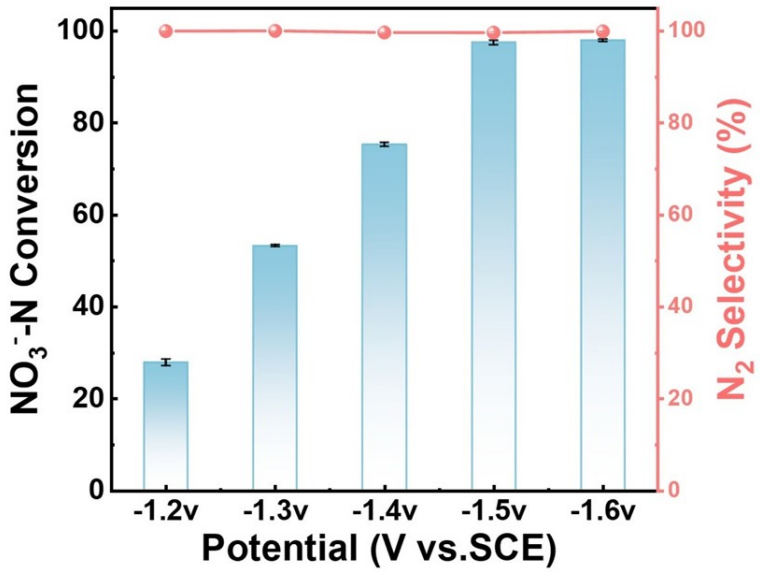

268

269 **Figure S20.** At different potentials by Co-OV/TiO_2@TP for 4h in 50 mg L^{-1} NO_3^--N, 0.03 M
270 KCl and 0.1 mol L^{-1} K_2SO_4 solution.

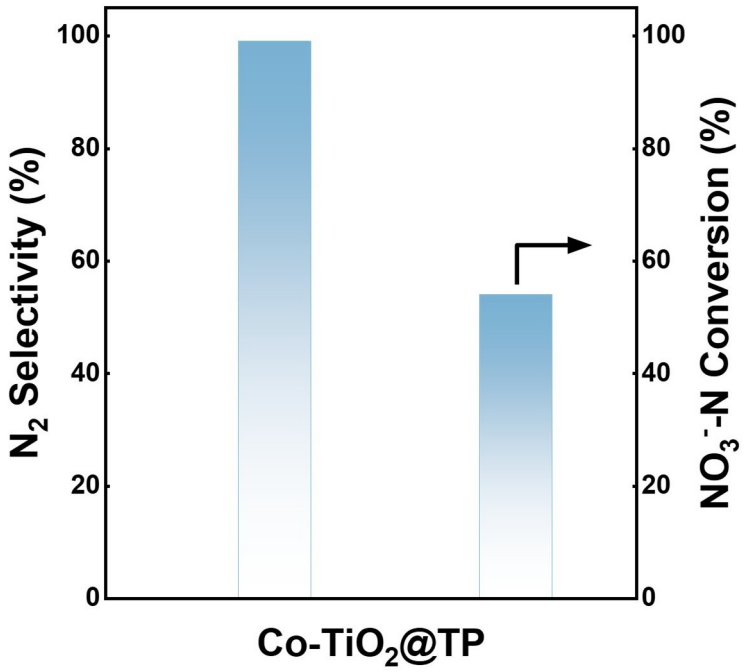

271

272 **Figure S21.** Photo-electrocatalytic NO_3^--N conversion and N_2 selectivity of Co-TiO_2@TP.

273

274

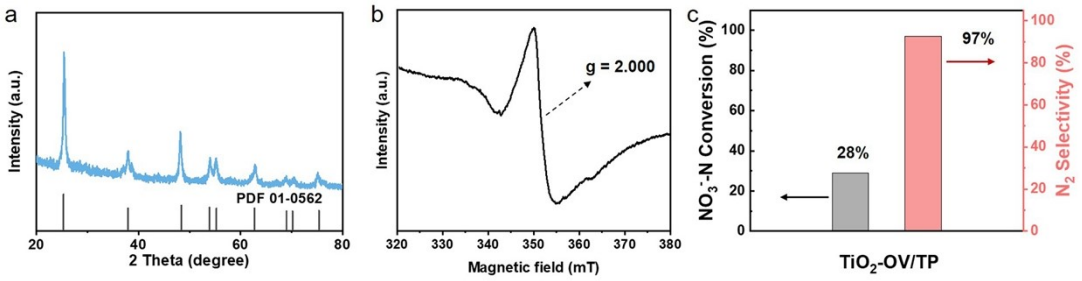

275

276 **Figure S22.** Characterization and NO_3RR performance of TiO_2-OV/TP prepared by Ar
277 calcination. (a) XRD pattern, (b) EPR spectrum, and (c) NO_3^--N conversion and N_2 selectivity.

278

279

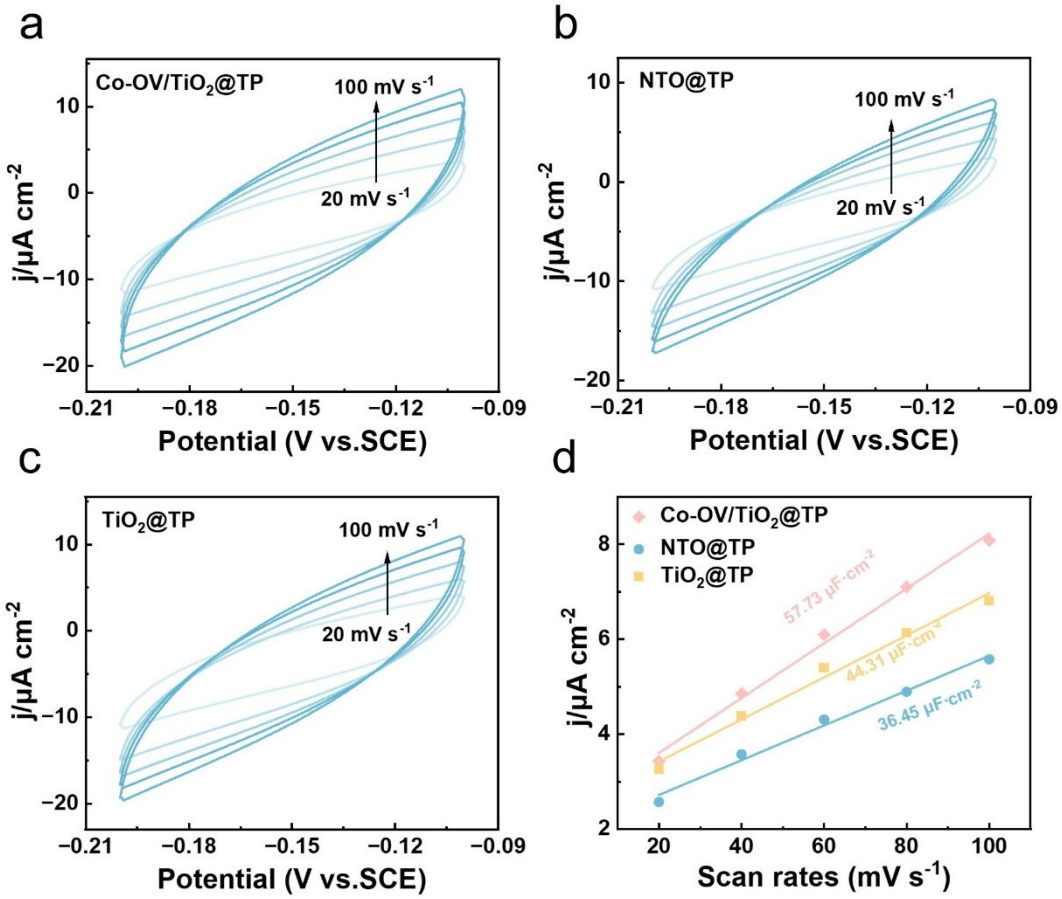

280

281 **Figure S23.** CV curves at the scan rates changed from 20 to 100 mV s^{-1}. Cyclic voltammetry
282 curves of (a) Co-OV/TiO_2@TP, (b) and NTO@TP (c) TiO_2@TP electrodes. (d) Plots of half of
283 the current density difference (Δj/2) at the centered potential plotted against the scan rate. The
284 slope of fitted straight line is the C_{dl} value.

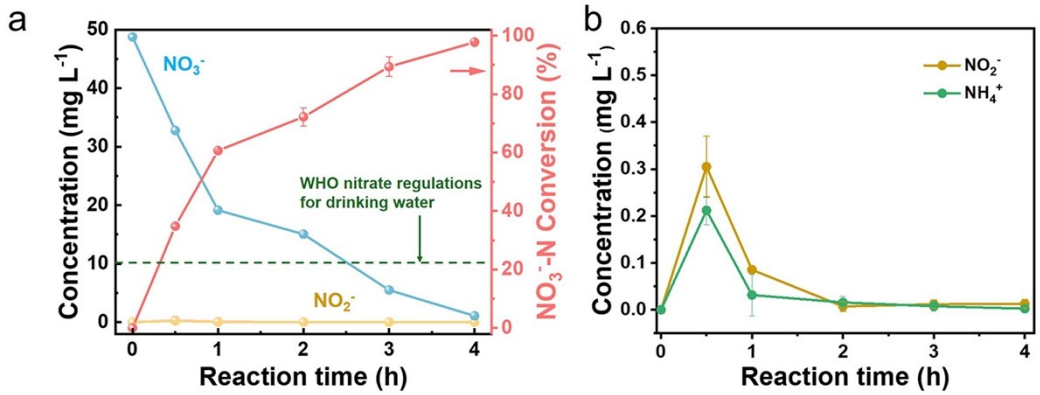

285

286 **Figure S24.** (a) Time-resolved concentration evolution of nitrogen species during the PEC
287 NO_3RR over Co-OV/TiO_2@TP at 1.5 V vs.SCE in 0.1 mol L^{-1} K_2SO_4 and 0.03 M KCl solution
288 with initial concentration of 50 mg L^{-1} NO_3^--N. The dashed line indicates the WHO drinking
289 water standard for nitrate (10 mg L^{-1} NO_3^--N). (b) The changes in the concentrations of
290 corresponding NO_2^- and NH_4^+ during the reaction process.

291 As shown in Figure S24a, the NO_3^--N concentration decreased steadily from 48.8 mg L^{-1} to 1.1
292 mg L^{-1} over 4 hours, corresponding to a conversion of ~98%. Meanwhile, NO_2^--N and NH_4^+-N
293 were identified as transient intermediates (Figure S24b), reaching maximum concentrations of
294 only ~0.3 mg L^{-1} and ~0.2 mg L^{-1}, respectively, at 0.5 h, and subsequently decaying rapidly to
295 near-zero levels (<0.1 mg L^{-1}) by the end of the reaction. The residual NO_2^--N and NH_4^+-N at
296 the reaction endpoint are both below the detection limit, and the nitrogen deficit (~98% of the
297 initial N) can be confidently attributed to N_2 generation.

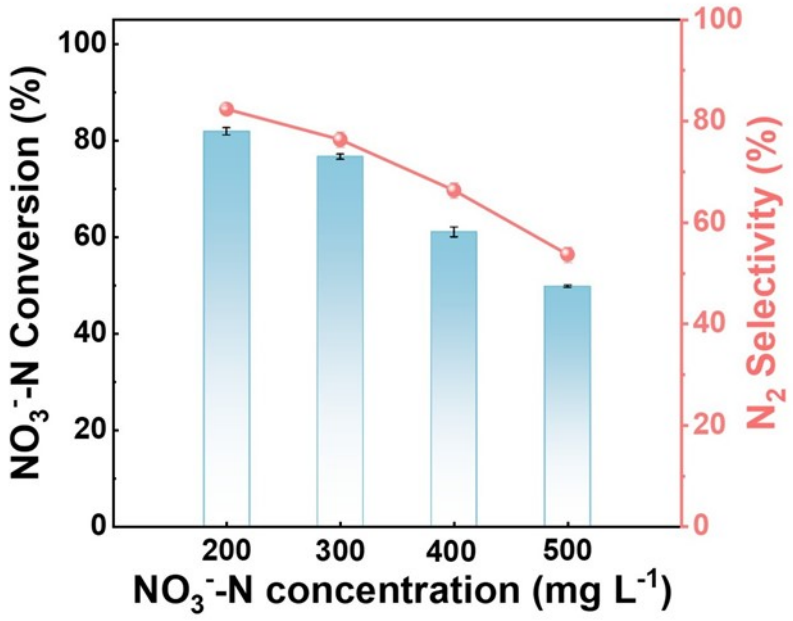

299

300 **Figure S25.** (a) The performance of Co-OV/TiO_2@TP under different initial concentration of
301 NO_3^--N.

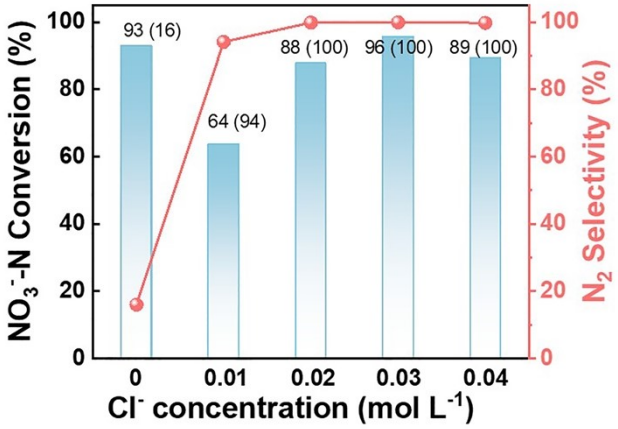

302

303 **Figure S26.** Effect of Cl^- concentration on the NO_3^--N conversion and N_2 selectivity of Co-
304 OV/TiO_2@TP under visible light irradiation at -1.5 V (vs. SCE).

305

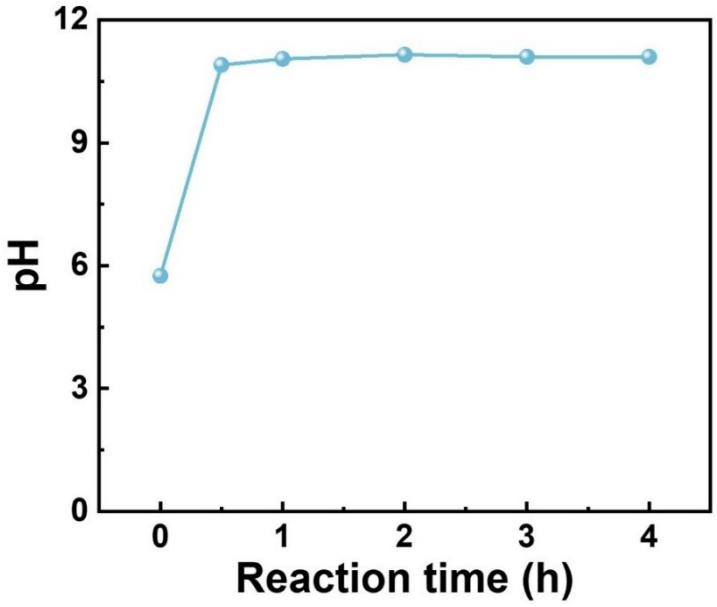

306

307 **Figure S27.** Time-dependent concentration changes of pH by Co-OV/TiO_2@TP at 1.5 V
308 vs.SCE in 0.1 mol L^{-1} K_2SO_4 and 0.03 M KCl solution with initial concentration of 50 mg L^{-1}
309 NO_3^--N.

310

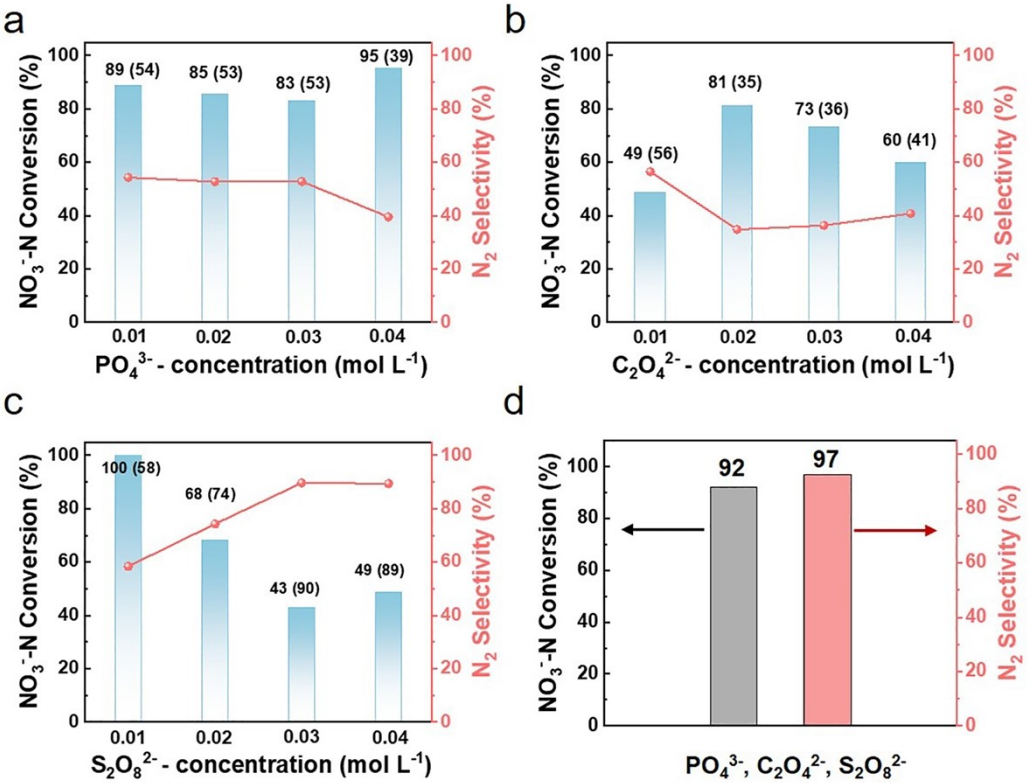

311

312 **Figure S28.** The catalytic performance of Co-OV/TiO_2@TP under different initial
313 concentration of (a) PO_4^{3-}, (b) $C_2O_4^{2-}$, (c) $S_2O_8^{2-}$ and (d) a mixture of $C_2O_4^{2-}$, PO_4^{3-} and $S_2O_8^{2-}$.

314 The three anions show distinctly different effects on Co-OV/TiO_2@TP. PO_4^{3-} exhibits the
315 mildest influence, with the NO_3^--N removal maintained at 83-95% across all tested
316 concentrations. $C_2O_4^{2-}$ shows a certain inhibitory effect with NO_3^--N removal of 49-81%, likely
317 due to competitive adsorption at active sites. $S_2O_8^{2-}$ displays a concentration-dependent
318 behavior, favoring NO_3^--N conversion at low concentrations and enhancing N_2 selectivity at
319 higher concentrations, reflecting its dual role in modulating both reduction and oxidation half-
320 reactions. These results confirm that the concentrations of coexisting anions indeed affect the
321 catalytic performance. More importantly, under a realistic multi-ion coexistence condition
322 (PO_4^{3-}, $C_2O_4^{2-}$, and $S_2O_8^{2-}$ with 0.03 mol L^{-1} Cl^-), Co-OV/TiO_2@TP still achieves 92% NO_3^--N
323 removal and 97% N_2 selectivity (Figure S28d). This can be possibly attributed to competitive
324 adsorption among the anions on the catalyst surface, which moderates the interference imposed
325 by any single species, confirming the strong anti-interference capability and practical
326 applicability of the proposed catalytic system.

327

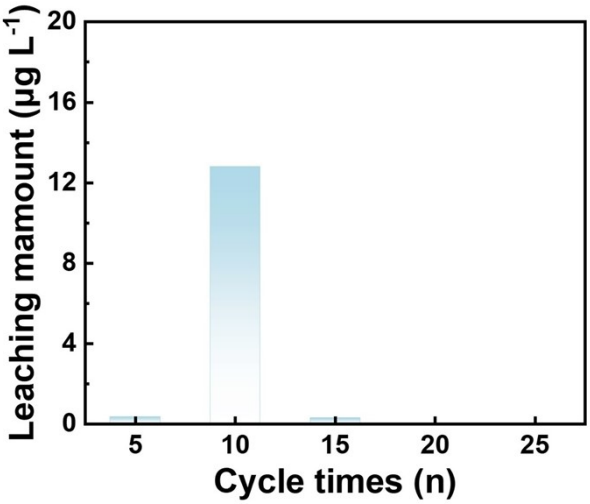

328

329 **Figure S29.** Co iron leaching amount of the Co-OV/TiO_2@TP cathode during 26 repeated
330 electrolysis tests (each test lasting 4 h).

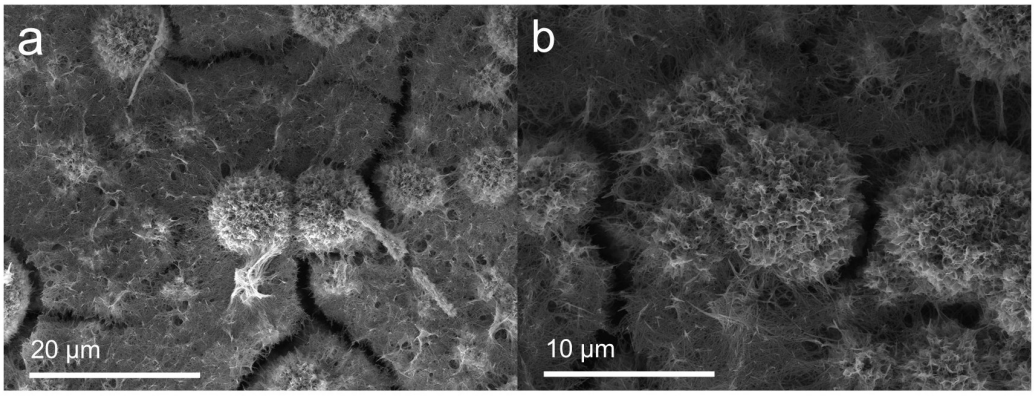

331

332 **Figure S30.** (a) SEM image of Co-OV/TiO_2@TP befer NO_3RR, (b) SEM image of Co-
333 OV/TiO_2@TP after NO_3RR.

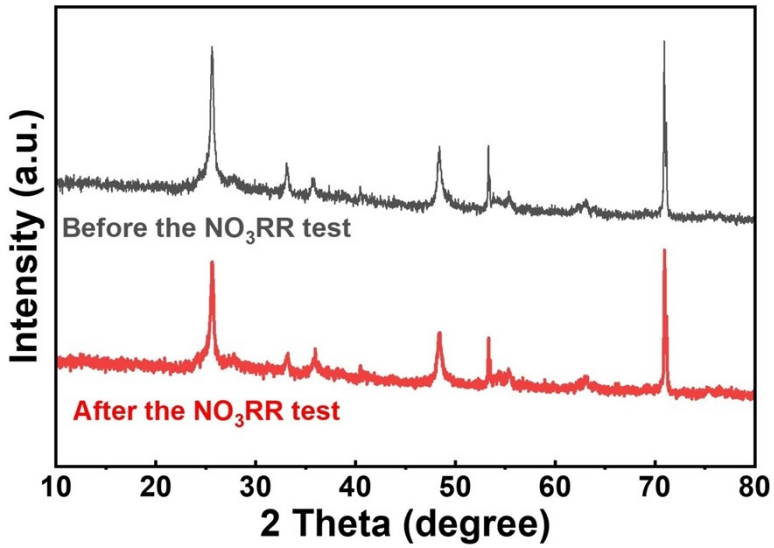

334

335 **Figure S31.** XRD patterns of Co-OV/TiO_2@TP after NO_3RR.

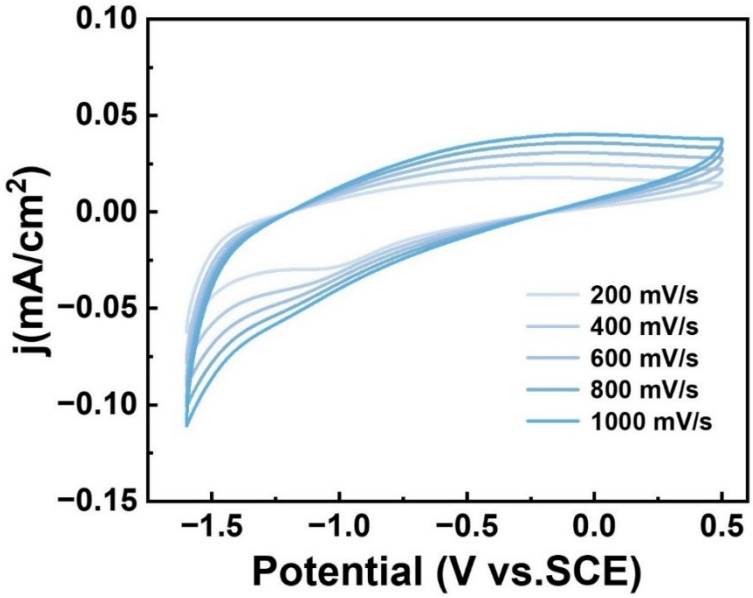

336

337 **Figure S32.** CV curves of NTO@TP with different scan rates.

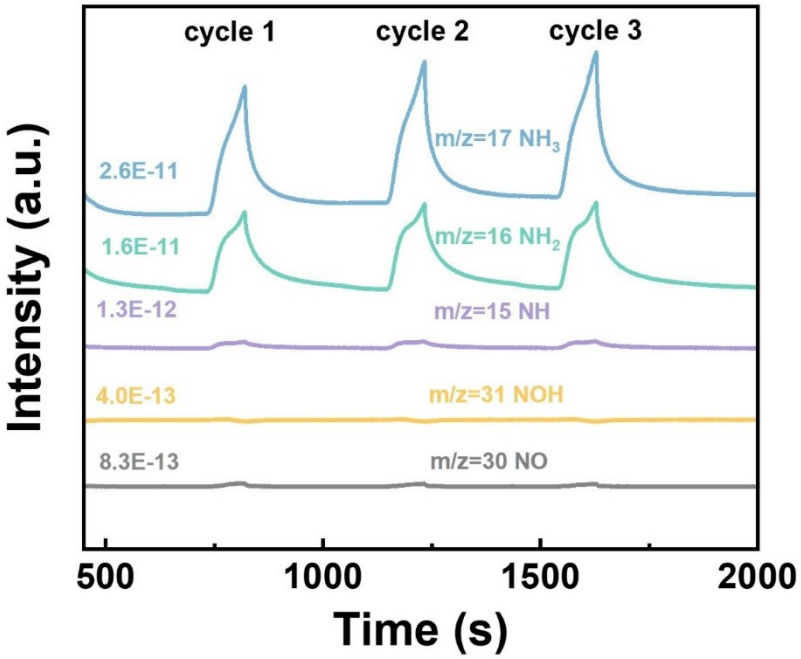

338

339 **Figure S33.** Electrochemical online DEMS results for the electrocatalytic NO_3RR over
340 NTO@TP.

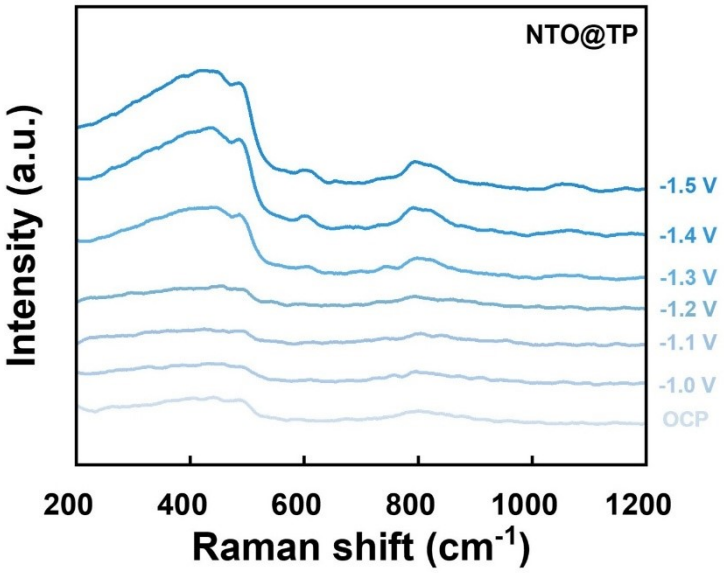

341

342 **Figure S34.** In situ Raman spectra of NTO@TP at different potentials.

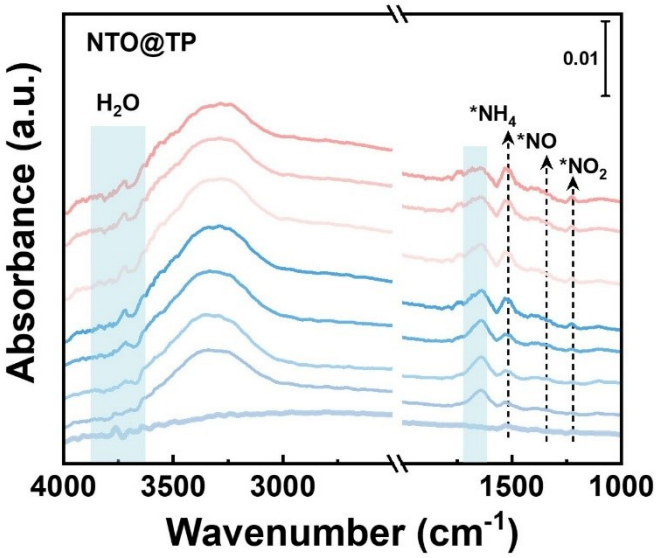

343

344 **Figure S35.** In situ electrochemical FT-IR spectra of NTO@TP at different potential.

345 **Table S1.** Comparison of NO_3RR performances with reported catalysts.

Catalysts	NO_3^--N (mg L^{-1})	NO_3^--N Conversion (%)	N_2 Selectivity (%)	Reaction conditions	Ref.
Co-OV/TiO_2@TP	50	98	100	PEC, visible light, -1.5 V (vs. SCE), 0.03 M Cl^-	**This work**
Cu_2O/TiO_2 NFs	100	90.2	98.7	EC, -1.3 V (vs. SCE), 0.1 M Na_2SO_4 + 0.04 M Cl^-, pH 7, 12 h	(6)
Ru_1Ni SAA	100	93	99	EC, -1.4 V (vs. SCE), Cl^-:SO_4^{2-} = 1:1 (total 0.2 M), pH 7, 9 h	(7)
PdCu-P_4/CS	100	96.3	95.2	PEC, 300 W xenon lamp (λ > 400 nm), -1.3 V (vs. SCE), 2 h	(8)
Pd-Cu NCs-NOMC	100	86	60	EC, -1.3 V (vs. SCE), 0.1 M Na_2SO_4 (neutral), 24 h	(9)

R-P25@Ag/Cu NPs	50	93	68	PC, 300 W Hg lamp, pH 3.5 (H_2SO_4), hole-scavenger-free, 180 min	(10)
$ZnSe/BiVO_4$	100	89.84	91.03	PC, 500 W Hg lamp (365 nm), HCOOH (50 mmol/L), pH 3.0, 50 min	(11)

References

[1] G. Kresse, D. Joubert, From ultrasoft pseudopotentials to the projector augmented-wave method, Physical Review B, 59 (1999) 1758-1775.

[2] G. Kresse, J. Furthmüller, J. Efficient iterative schemes for ab initio total-energy calculations using a plane-wave basis set. Physical Review B, *54* (1996), 11169-11186.

[3] G. Kresse, J. Furthmüller, Efficiency of ab-initio total energy calculations for metals and semiconductors using a plane-wave basis set, Computational Materials Science, 6 (1996) 15-50.

[4] J.P. Perdew, K. Burke, M. Ernzerhof, Generalized Gradient Approximation Made Simple [Phys. Rev. Lett. 77, 3865 (1996)], Physical Review Letters, 78 (1997) 1396-1396.

[5] H.J. Monkhorst, J.D. Pack, Special points for Brillouin-zone integrations, Physical Review B, 13 (1976) 5188-5192.

[6] Y. Cong, X. Kang, Z. Wu, L. Gu, C. Wu, X. Duan, J. Chen, J. Yang, Self-Reconstruction Induced Electronic Metal-Support Interaction for Modulated Cu^{+} Sites on TiO_2 Nanofibers in Electrocatalytic Nitrate Conversion, Small, 20 (2024) 2407554.

[7] Z. Wu, X. Kang, S. Wang, Y. Song, F. Xie, X. Duan, J. Yang, Co-Catalytic Metal-Support Interactions Design on Single-Atom Alloy for Boosted Electro-Reduction of Nitrate to Nitrogen, Advanced Functional Materials, 34 (2024) 2406917.

[8] J. Sun, H. Yang, W. Gao, T. Cao, G. Zhao, Diatomic Pd−Cu Metal-Phosphorus Sites for Complete N≡N Bond Formation in Photoelectrochemical Nitrate Reduction, Angewandte Chemie International Edition, 61 (2022) e202211373.

[9] H. Xu, H. Xu, Z. Chen, X. Ran, J. Fan, W. Luo, Z. Bian, W.X. Zhang, J. Yang, Bimetallic PdCu Nanocrystals Immobilized by Nitrogen-Containing Ordered Mesoporous Carbon for Electrocatalytic Denitrification, ACS Appl Mater Interfaces, 11 (2019) 3861-3868.

[10] C. Wang, S. Dong, Y. Wang, T. Guo, G. Gao, Z. Lu, B. Pan, Selective removal of nitrate

via the synergistic effect of oxygen vacancies and plasmon-induced hot carriers, Chemical Engineering Journal, 397 (2020) 125435.

[11] H. Shi, C. Li, L. Wang, W. Wang, J. Bian, X. Meng, Photocatalytic reduction of nitrate pollutants by novel Z-scheme ZnSe/$BiVO_4$ heterostructures with high N_2 selectivity, Separation and Purification Technology, 300 (2022) 121854.